A Grating Coupler Design for Optical Vortex Mode Generation in Rectangular Waveguides

Denis M. Fatkhiev, *Member, IEEE*, Vladimir S. Lyubopytov, *Member, IEEE*, Ruslan V. Kutluyarov, *Member, IEEE*, Elizaveta P. Grakhova, and Albert K. Sultanov

***Abstract*—We propose and numerically verify a design approach to a grating coupler (GC) for in-plane generation and propagation of quasi-TE vortex modes with azimuthal order ± 1 within photonic integrated circuits (PICs). In the considered GC design example, silicon nitride waveguides with silica substrate and cladding are used. The shallowly etched grating is illuminated by the incident optical beam from a standard single-mode fiber. We optimize the GC design parameters to maximize the purity of orbital angular momentum (OAM) mode first for the case of a theoretical ideally fabricated grating, and then consider a more practical case of GC design, when the etching resolution is limited. The numerical modeling results show possibility of the vortex mode generation with $>96\%$ purity of the target OAM state ± 1 at the wavelength 1550 nm. The proposed design, compatible with the standard nanofabrication process, provides a simple, compact and robust solution for various potential PIC-based applications of OAM beams.**

***Index Terms*—Optical waveguides, orbital angular momentum, silicon nitride, vortex beam, waveguide gratings.**

I. Introduction

OPTICAL vortex beams, i.e., the light beams with a helical phase front, are known to carry an orbital angular momentum (OAM) of $\ell\hbar$ per photon, where integer ℓ is the topological charge of vortex beam and $\hbar$ is the Planck constant [1]. Optical vortices, carrying distinct OAM, form a theoretically unlimited basis of orthogonal functions. These remarkable properties of vortex beams make their employment beneficial for a number of existing and envisioned applications, such as high data rate classical optical communications over optical fiber [2], [3] and free-space links [4]–[6], optical tweezers and spanners [7]–[9], imaging and microscopy [10]–[12], quantum entanglement [13], [14], remote sensing [15], etc. The growing number of tasks that can be solved using optical vortices require more advanced and efficient methods for their generation and transmission.

Manuscript received February 24, 2021; revised June 2, 2021; accepted June 12, 2021. Date of publication June 15, 2021; date of current version July 7, 2021. This work was supported under the Grant of the Russian Science Foundation (Project No. 19-49-04112). *(Corresponding author: Denis M. Fatkhiev.)*

Denis M. Fatkhiev, Ruslan V. Kutluyarov, Elizaveta P. Grakhova, and Albert K. Sultanov are with the Telecommunication Systems Department, Ufa State Aviation Technical University, Ufa 450008, Russia (e-mail: fatkhiev.dm@gmail.com; kutluyarov@gmail.com; eorlingsbest@mail.ru; tks@ugatu.ac.ru).

Vladimir S. Lyubopytov is with the Center for Photonics and Quantum Materials, Skolkovo Institute of Science and Technology, Moscow 121205, Russia and also with the Telecommunication Systems Department, Ufa State Aviation Technical University, Ufa 450008, Russia (e-mail: v.lyubopytov@skoltech.ru).

Digital Object Identifier 10.1109/JPHOT.2021.3089664

Typically, vortex beams can be generated and detected using discrete optical devices including diffractive optical elements [16], cylindrical lens mode converters [17], spiral phase plates [18], and holograms programmed on spatial light modulators [19]. However, in recent years, solutions based on photonic integrated circuits (PICs) have attracted the greatest interest due to their energy efficiency, compactness, high radiation performance, and repeatability in mass fabrication due to available technological processes.

The PIC-based solutions for optical vortices generation can be divided into two groups: out-of-plane solutions, and in-plane solutions. The out-of-plane approach implies the principles of scattered field generation based on microring resonators with angular gratings [20], [21], free-form metasurfaces [22], micro spiral phase plates placed at the output port of a vertical-cavity surface-emitting laser [23], annular grating [24], [25], or two-dimensional fiber-gratings [26]. This approach has shown robustness and high purity of the generated OAM states, allowing OAM-multiplexed data transmission [27], [28]. However, in this case, the vortex beam is generated in free space, and to couple it into a fiber or another PIC generally a lens is needed. The need for free-space components affects the reliability, functionality, and size of the final device.

In turn, the in-plane solutions provide the vortex mode generation and propagation inside the dielectric waveguide, bringing the advantageous possibility to implement a vortex emitter as part of more complex integrated devices for processing or (de)multiplexing OAM-carrying optical signals on a chip. Additionally, the in-plane design opens a possibility to couple the output beam to the fiber using an effective edge-coupling scheme.

There are several theoretical design proposals for the integrated devices intended for in-plane vortex mode generation in the waveguides. In [29] a rectangular waveguide based on a Silicon-On-Insulator (SOI) platform with a single longitudinal trench is used to split the mode degeneracy and excite two orthogonal LP-like eigenmodes with different propagation constants for further synthesis of a vortex beam. Another idea is to use hybrid plasmonic waveguides, e.g. in [30] the copper layer is located on top of the silicon nanowire with silica spacer between them; in [31] L-shaped asymmetric copper strip is located on the right top of the square silicon core; a scheme in [32] applies graphene hybrid waveguide for a quasi-linear mode conversion into a quasi-circular mode in a dynamic tuning manner. It should be noted that in the last three cases the OAM beam is represented by the longitudinal component of the electric field,

which complicates its application. Another technique utilizes a metasurface for coupling incident radiation into an integrated waveguide [33]. The metasurface is represented by a silicon antenna array placed on the surface of the Si_3N_4 waveguide. To summarize, the devices based on hybrid plasmon waveguides and metasurfaces are very compact but are not straightforwardly compatible with the commercially available PIC technological platforms. Such compatibility is provided by the design proposed in [34]: radiation is injected into two waveguides using edge-couplers to form TE_{10} and TE_{01} modes, which are subsequently combined with a $\pi/2$ or $-\pi/2$ phase shift. However, to obtain a vortex beam, the TE_{00} and TM_{00} modes are required to be simultaneously introduced via edge-couplers, which represents certain technological inconveniences.

In this paper, we propose a very simple and compact structure for in-plane generation of quasi-TE vortex mode with azimuthal order $\ell = \pm 1$, compatible with the standard nanofabrication process and existing photonic integration platforms. In our scheme, the vortex mode is generated in the waveguide directly from the beam incident to the grating coupler (GC) from a standard single-mode fiber (SMF). The paper is organized as follows: in Section II, we describe the general design concept of the proposed integrated device and its operation principle, and also formulate the problem of the device parameters optimization; in Section III, based on the numerical modeling results, we define the design parameters for an exemplary device based on silicon nitride PIC platform, and theoretically analyze the performance of the considered device; and in Section IV we discuss the results and make conclusions.

II. Design Concept and Operation Principle

As we have shown in [35], in dielectric rectangular waveguides quasi-degenerate vortex modes with azimuthal order $\pm\ell$ can be supported as the following superpositions of quasi-TE or quasi-TM eigenmodes:

$$\mathbf{E}_{\pm\ell}(x,y,z) = -i^{\ell}\sum_{j=0}^{\ell}(\pm i)^{j}\mathbf{E}_{j,\ell-j}(x,y)exp(-j\beta_{j,\ell-j}z), \tag{1}$$

where the subscripted spatial indices μ and ν of the eigenmode electric field vector $\mathbf{E}_{\mu\nu}$ denote the number of phase inversions in the dominant electric field component over x and y axes, respectively. However, the phase-matching condition between the constituent eigenmodes providing a stable helical phase front over the waveguide can be achieved only for the case $\ell = \pm 1$. In this case, for equation (1) we have:

$$\mathbf{E}_{\pm 1} = -i\mathbf{E}_{01} \pm \mathbf{E}_{10}. \tag{2}$$

Therefore, the generation of the vortex mode in a waveguide directly from a single incident beam can be reached by simultaneous generation of the waveguide eigenmode fields $\mathbf{E}_{01}$ and $\mathbf{E}_{10}$ with equal intensities and an appropriate phase shift. In that way, the proposed GC design essentially is formed as a superposition of two sub-gratings, each of which is intended for excitation of the waveguide eigenmode fields $\mathbf{E}_{01}$ and $\mathbf{E}_{10}$, respectively. Here we focus on quasi-TE waveguide modes due to their efficient coupling via GCs, typically lower insertion losses in waveguides and other passive components, and the variety of building blocks optimized for a quasi-TE mode in the existing PIC platforms. To keep the GC possibly simple to fabricate and compatible with the standard integration process, the GC is supposed to have one etching depth. Therefore, the sub-gratings are superimposed with the following rule: in each point at the GC surface, if at least one of the sub-gratings has a groove, then the resulting GC should also have a groove with the standard etching depth; and if neither of the sub-gratings has a groove, then the resulting GC should not be etched in that point (see Fig. 1).

As a target waveguide enabling the vortex mode generation and transmition, we consider the symmetric (surrounded by silica) silicon nitride waveguide, the geometry of which is optimized in [35] for the propagation of quasi-degenerate quasi-TE vortex mode with azimuthal order $\ell = \pm 1$. In this case, the target waveguide has a size of 1370×1250 nm^2, and both constituent eigenmodes TE_{10} and TE_{01} have effective indices of around 1.6887. Fig. 2 shows the layout sketch of the device under consideration composed of the GC irradiated by the SMF, the target waveguide, and a linear taper for adiabatic coupling between them. According to the planar technology, all sections of this device should have the same height dictated by the target waveguide, the heigth of which equals 1250 nm in order to support the TE_{01} eigenmode.

First, we model and preliminarily optimize the sub-gratings for the generation of the TE_{10} and TE_{01} eigenmodes separately. The first one consists of two semi-gratings longitudinally shifted relative to each other for a half-period (see Fig. 1). This structure is intended to support the π phase shift between two lobes of the dominant electric field component E_x of the TE_{10} eigenmode. For the second one, we use the typical grating structure with the period providing the phase-matching condition for the TE_{01} eigenmode. The etching depth for both sub-gratings is set to 30%, which is a typical value for shallowly etched gratings (for the waveguide height of 1250 nm, this equals 375 nm).

For optimization of sub-gratings, we consider the purity of the target eigenmodes as the main objective function, and the overall coupling efficiency as a secondary one. Ansys Lumerical FDTD Solver has been used for all calculations of the electromagnetic (EM) fields. The calculations were carried out on a various two-processor nodes of the USATU (Ufa State Aviation Technical University) computing cluster mainly using Intel Xeon Gold 6126, 5222 and 6226 processors. The computation time required to complete the optimization of GC from scratch is about 40 hours.

The FDTD calculation area is $40\times7.625\times24$ μm^3 with the non-uniform grid with the maximum mesh size $50\times20\times50$ nm^3, minimum mesh step 0.25 nm, and time step 0.057 fs. The SMF has a mode field diameter of 10.4 μm at 1550 nm, and its facet is placed at the height of 200 nm over the silica cladding.

To assess the purity of generated eigenmodes, the expansion coefficients of the output electric field vector $\mathbf{E}(\mathbf{r})$ over the basis of the waveguide eigenmode electric field vectors $\mathbf{E}_{\mu\nu}(\mathbf{r})$ were determined using Python as follows:

$$a_{\mu\nu} = \iint_{\mathbf{R}^2}\mathbf{E}^{*}_{\mu\nu}(\mathbf{r})\mathbf{E}(\mathbf{r})d^2\mathbf{r}, \tag{3}$$

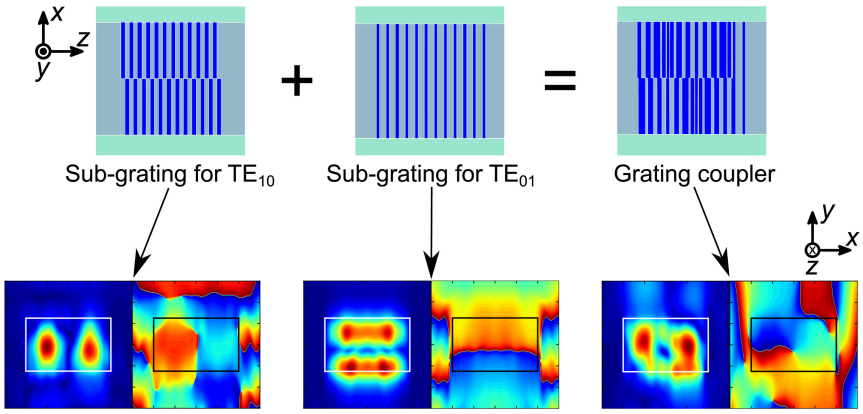

Fig. 1. Schematic representation of the GC formation by superimposing the sub-gratings.

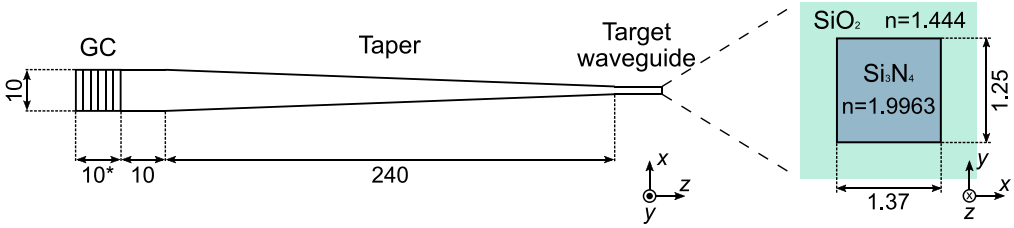

Fig. 2. Sketch of the device layout and the target waveguide cross-section; dimensions are shown in μm; * denotes the minimum GC length, because the actual value is defined by the integer number of periods in the sub-gratings and the longitudinal shift between them.

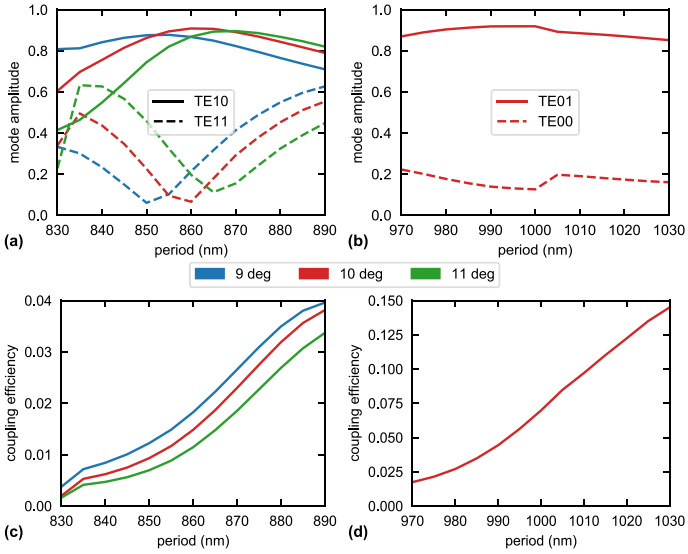

Fig. 3. Amplitude of the modal decomposition coefficients for the target eigenmode and the next highest parasitic eigenmode at the output of the sub-gratings generating eigenmodes TE_{10} (a) and TE_{01} (b) vs. the sub-grating period; overall coupling efficiency for the sub-gratings generating eigenmodes TE_{10} (c) and TE_{01} (d) vs. the sub-gratings period.

where $\mathbf{r} = (x, y)$ is the radius vector, and integration is performed over the cross-section of 40×5 $\mu\mathrm{m}^2$ within the calculated FDTD area.

Fig. 3 shows the resulting modal decomposition coefficients and the overall coupling efficiency after the sub-gratings generating TE_{10} and TE_{01} eigenmodes, depending on the sub-grating period. Here and in the following calculations, we assume the radiation wavelength is 1550 nm. Both sub-gratings have a filling factor (i.e., the fraction of the remaining full-height waveguide length within the period) $\Gamma = 0.5$, which is supposed to provide maximum coupling efficiency. The simulation results confirm that the generation of a pure TE_{10} eigenmode is less effective compared to TE_{01}. This is caused by the parasitic generation of TE_{11} eigenmode, which prevents using the range of periods providing the highest coupling efficiency. TE_{11} mode is inevitably supported by the waveguide of the considered height, and its generation is allowed by the geometry of the sub-grating intended for TE_{10} mode generation. However, the coupling of the other eigenmodes supported by the waveguide is prohibited by this sub-grating, so they have a negligible impact on the output modal content. Therefore, due to the lower performance, this sub-grating is set determinative for optimizing the fiber tilt angle. Considering together the TE_{10} mode purity and the overall coupling efficiency (see Fig. 3 [a],[c]), the fiber tilt angle of 10° to the surface normal was chosen. To achieve the highest purity of the target eigenmodes, the periods Λ of the sub-gratings generating modes TE_{10} and TE_{01} have been determined around 860 nm and 1000 nm, respectively.

As the coupling efficiencies of the sub-gratings are considerably different, to match them according to (2), the filling factor can be varied. For the sub-grating generating TE_{10} eigenmode, which has lower performance, we set the filling factor $\Gamma_{\mathrm{TE}_{10}} = 0.5$ and the period $\Lambda_{\mathrm{TE}_{10}} = 860$ nm to keep as much as possible its coupling efficiency and mode purity. For the sub-grating generating TE_{01} eigenmode, we increase the filling factor and fine-tune the period to adjust its coupling efficiency and minimize the generation of unwanted modes. To achieve the required phase shift of $\pm\pi/2$ between the constituent

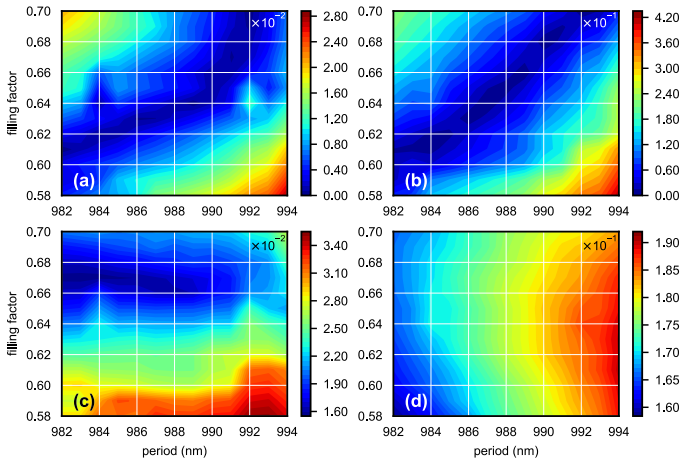

Fig. 4. Coupling imbalance (a) and phase mismatch between the TE_{10} and TE_{01} eigenmodes (b), parasitic coupling efficiency (c), and useful coupling efficiency (d) of the GC vs. the period $\Lambda_{TE_{01}}$ vs. the filling factor $\Gamma_{TE_{01}}$ of the sub-grating generating eigenmode TE_{01} for the GC with ideal etching resolution, designed for the target OAM state +1. The longitudinal shift $\Delta_{TE_{01}}$ is fixed to + 235 nm.

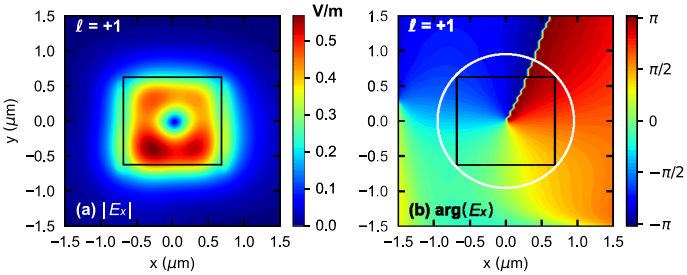

Fig. 5. Numerically calculated absolute amplitude distribution (a) and phase distribution (b) of the E_x field component in the target waveguide for the GC with ideal etching resolution, designed for OAM state +1. White circumference shows the area considered for OAM spectrum calculation.

TABLE I
OPTIMIZED GC DESIGN PARAMETERS

Target OAM state	Etching resolution	$\Lambda_{TE_{01}}$, nm	$\Gamma_{TE_{01}}$, nm	$\Delta_{TE_{01}}$, nm
+1	unlimited	991	0.68	-235
+1	100 nm	987	0.64	-275
-1	100 nm	991	0.65	+225

eigenmodes, we longitudinally shift the sub-gratings relative to each other.

Therefore, there is a set of three geometric parameters of the sub-grating generating TE_{01} mode: period $\Lambda_{TE_{01}}$, filling factor $\Gamma_{TE_{01}}$, and longitudinal shift $\Delta_{TE_{01}}$, which define the performance of the resulting GC in respect to OAM mode generation. From the physical point of view, we assume that these parameters influence the GC operation mainly as follows:

1) period $\Lambda_{TE_{01}}$ determines the coupling efficiency and the mode purity of the TE_{01} eigenmode;
2) filling factor $\Gamma_{TE_{01}}$ determines the coupling efficiency of the TE_{01} eigenmode;
3) longitudinal shift $\Delta_{TE_{01}}$ determines the relative phase shift between the TE_{01} and TE_{10} eigenmodes.

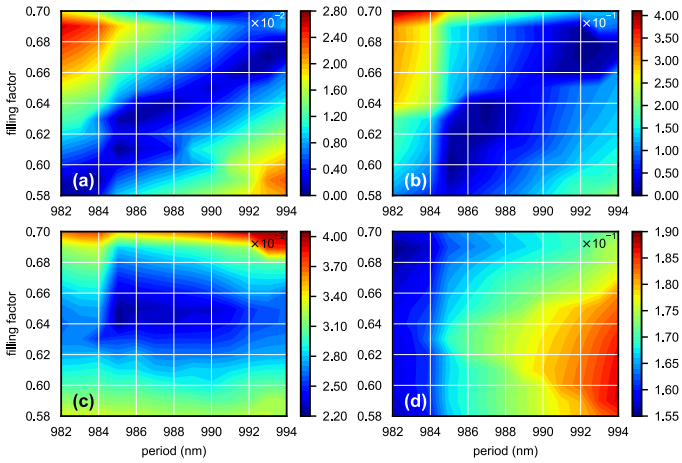

Fig. 6. Coupling imbalance (a) and phase mismatch between the TE_{10} and TE_{01} eigenmodes (b), parasitic coupling efficiency (c), and useful coupling efficiency (d) vs. the period $\Lambda_{TE_{01}}$ vs. the filling factor $\Gamma_{TE_{01}}$ of the sub-grating generating eigenmode TE01 for the GC with the limited resolution, designed for the target OAM state +1. The longitudinal shift $\Delta_{TE_{01}}$ here is fixed to -275 nm.

However, these parameters also influence the effective indices n_{eff} of both the TE_{10} and TE_{01} eigenmodes propagating in the GC. As the optimal values of these parameters ourselves intrinsically depend on the effective indices of eigenmodes, only simultaneous optimization of these parameters is possible.

Therefore, these parameters form a 3-dimensional space of input vectors, over which we define a set of four objective functions, characterizing the GC performance in terms of the 1st order OAM mode generation:

1) coupling imbalance between the TE_{10} and TE_{01} eigenmodes, i.e., an absolute difference of the coupling efficiencies for the TE_{10} and TE_{01} eigenmodes in the target waveguide:

$$\eta_{\text{diff}} = |\eta_{TE_{10}} - \eta_{TE_{01}}| \rightarrow min, \tag{4}$$

2) phase mismatch between the TE_{10} and TE_{01} eigenmodes, i.e., an absolute value of the deviation of the phase difference between E_x components of TE_{10} and TE_{01} eigenmodes at the input of the target waveguide from $\pm\pi/2$:

$$\Delta\varphi = |arg(E_{xTE_{10}}) - arg(E_{xTE_{10}}) \pm \pi/2| \rightarrow min, \tag{5}$$

3) the parasitic coupling efficiency of the GC, i.e., the total coupling efficiency except for TE_{10} and TE_{01} eigenmodes:

$$\eta_{\text{par}} = (\eta - \eta_{TE_{10}} - \eta_{TE_{01}}) \rightarrow min, \tag{6}$$

4) the useful coupling efficiency of the GC, i.e., the sum of coupling efficiencies for TE_{10} and TE_{01} eigenmodes at the input of the target waveguide:

$$\eta_{\text{sum}} = (\eta_{TE_{10}} + \eta_{TE_{01}}) \rightarrow max, \tag{7}$$

Here these optimization criteria are put in an order of descending priority. This order defines our preference for the solutions to this optimization problem.

TABLE II
CALCULATED GC PERFORMANCE CHARACTERISTICS AT THE TARGET WAVELENGTH 1550 NM

Target OAM state	Etching resolution	Normalized output power	Normalized OAM power distribution of the output fields component E_x						
			-3	-2	-1	0	+1	+2	+3
+1	unlimited	0.0235	0.00131	0.00116	0.00006	0.00372	**0.97379**	0.00321	0.00006
+1	100 nm	0.0226	0.00129	0.00280	0.00016	0.00394	**0.96748**	0.00338	0.00012
-1	100 nm	0.0228	0.00010	0.00461	**0.96583**	0.00542	0.00008	0.00174	0.00132

III. NUMERICAL SIMULATION RESULTS

A. Optimization of the GC With Ideal Etching Resolution

First, let us consider the idealized case when the minimum size of the grating features is not limited. To find the optimal values of $\Lambda_{\mathrm{TE}_{01}}$, $\Gamma_{\mathrm{TE}_{01}}$, and $\Delta_{\mathrm{TE}_{01}}$, we calculate the EM field at the output of GC illuminated by the field from SMF using Lumerical FDTD, and decompose it according to (3).

During GC optimization, we assume adiabatic operation of the taper, i.e., mode coupling in the taper is neglected. We model the taper operation over TE_{10} and TE_{01} eigenmodes by a 2×2 diagonal complex scattering matrix. To find this S-matrix, we calculate the EM field at the taper output when it is excited by TE_{10} and TE_{01} eigenmodes separately with equal normalized intensity and make modal decomposition of the resulting fields. Then this S-matrix is applied to the complex vector of modal coefficients $(a_{\mathrm{TE}_{10}}, a_{\mathrm{TE}_{01}})^T$, calculated for the EM field at the GC output according to (3), and the resulting vector is used to determine the values of η_{diff}, η_{sum}, and $\Delta\varphi$.

To coarsely find the regions of values for period $\Lambda_{\mathrm{TE}_{01}}$, filling factor $\Gamma_{\mathrm{TE}_{01}}$, and longitudinal shift $\Delta_{\mathrm{TE}_{01}}$, we run several iterations of GC simulation gradually improving the set of these GC parameters towards their optimized values. Then, for fine adjustment of the GC parameters, we run 2-dimensional sweeps of period $\Lambda_{\mathrm{TE}_{01}}$ and filling factor $\Gamma_{\mathrm{TE}_{01}}$ around their course values at fixed values of longitudinal shift $\Delta_{\mathrm{TE}_{01}}$. Fig. 4 shows the resulting contour plots of the objective functions for the case $\ell = +1$.

According to our preference, we chose the following optimized parameters of GC: $\Lambda_{\mathrm{TE}_{01}} = 991$ nm, $\Gamma_{\mathrm{TE}_{01}} = 0.68$, $\Delta_{\mathrm{TE}_{01}} = -235$ nm (see Table I). The period and filling factor for the sub-grating generating eigenmode TE_{10} have been previously defined as $\Lambda_{\mathrm{TE}_{10}} = 860$ nm and $\Gamma_{\mathrm{TE}_{10}} = 0.5$. Fig. 5 shows the amplitude and phase distributions of the dominant electric field component E_x of the resulting EM field in the target waveguide.

To quantitatively estimate the distribution of OAM states carried by the calculated quasi-degenerate mode in the target waveguide, we expand its dominant electric field component E_x over the basis of angular harmonics [36] using MATLAB:

$$\psi_\ell = \int_{-\pi}^{+\pi} E_x(\varphi) e^{-i\ell\varphi} d\varphi. \tag{8}$$

For the expansion calculation, we consider the circular area, centered at the central point of the waveguide cross-section and confined by the radius, at which the amplitude of E_x falls to $1/e$ of its maximum value (see Fig. 5). The resulting normalized power distributions of OAM states are summarized in Table II

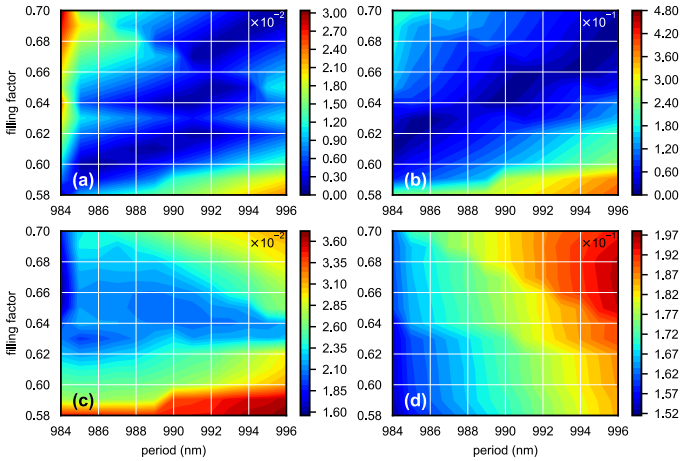

Fig. 7. Coupling imbalance (a) and phase mismatch between the TE_{10} and TE_{01} eigenmodes (b), parasitic coupling efficiency (c), and useful coupling efficiency (d) vs. the period $\Lambda_{\mathrm{TE}_{01}}$ vs. the filling factor $\Gamma_{\mathrm{TE}_{01}}$ of the sub-grating generating eigenmode TE01 for the GC with the limited resolution, designed for the target OAM state -1. The longitudinal shift $\Delta_{\mathrm{TE}_{01}}$ here is fixed to +225 nm.

(for brevity, we show the values for the target OAM state $+1$ and the next largest values, corresponding to the OAM states from –3 to -3). As can be seen, the generated mode carries the target OAM state $+1$ to an extent >97% by power with high purity. For the case of target OAM state $\ell = -1$, the GC can be optimized similarly.

B. Optimization of the GC With Limited Etching Resolution

As the optimal values of the GC parameters are interrelated via effective indices of the TE_{10} and TE_{01} eigenmodes, and the effective indices depend on the GC layout, for any specific value of etching resolution the optimization procedure is required, as described in Section III-A.

Noteworthy, in the proposed GC design, the minimum size of features to be etched is defined as $(1 - \Gamma_{\mathrm{TE}_{01}}) \cdot \Lambda_{\mathrm{TE}_{01}}$, i.e., it is about the typical feature size of grating couplers. Therefore, we assume that all the etched areas in the GC design are supported by the technological process. However, the remaining ridges of the full waveguide height in the GC design may have an arbitrarily small size. Therefore, in course of fabrication, the size of these GC areas may be affected by the technological process limitations, e.g., the lithography resolution or/and photoresist properties. As an example, let us consider the minimum feature size for the remaining waveguide ridges to be 100 nm. Therefore, at each iteration during GC optimization, in the corresponding

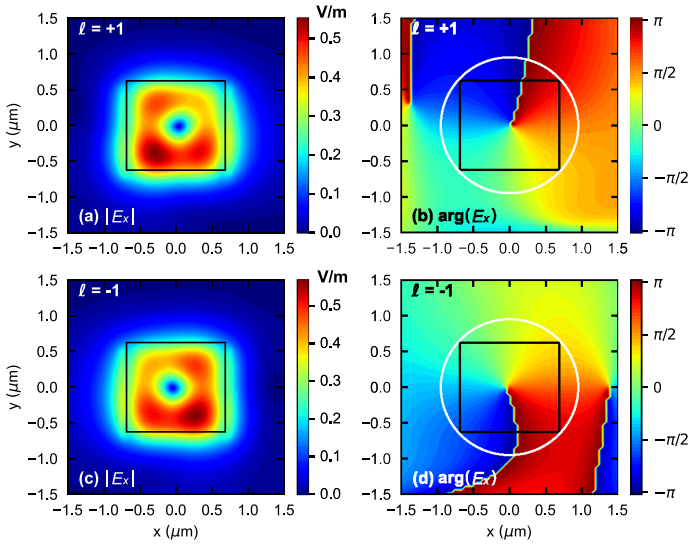

Fig. 8. Numerically calculated absolute amplitude distributions (a, c) and phase distributions (b, d) of the E_x field component in the target waveguide for the GC with the limited resolution, designed for the target OAM states $+1$ (a, b) and -1 (c, d). White circumference shows the area considered for OAM spectrum calculation.

GC design, all the ridges thinner than this given minimum feature size are removed.

Figs. 6 and 7 show the resulting contour plots for the objective functions (4)–(7) for the cases $\ell = \pm 1$, respectively. As can be seen, the limited minimum feature size may lead to nonmonotonic dependence of the objective functions on the input GC parameters within certain regions. This is caused by the sharp changes in the effective indices of eigenmodes when removing from the GC design the grating ridges thinner than the minimum supported feature size. As a result, the optimization process may become more complicated, and obviously, with increasing the minimum supported feature size, the optimization of GC parameters will become less effective.

For the considered minimum feature size of 100 nm, we choose as optimal the GCs parameters based on the simulation results and our preference, which are summarized in Table I. The corresponding calculated transverse electric field distributions in the target waveguide are shown in Fig. 8. Table II summarizes the corresponding normalized OAM power distributions for the target OAM states ± 1 and the next highest OAM components, as well as the total output power in the target waveguide normalized to the input power from SMF (overall coupling efficiency).

C. Optical Bandwidth Analysis

To estimate the optical broadbandness of the designed integrated devices, we calculated the output EM field in the target waveguide at the wavelengths ± 5 nm and ± 10 nm to the target wavelength, the corresponding OAM spectra, and the coupled output power. Fig. 9 shows the resulting graphs for the target OAM state purity and the normalized total output power for the devices generating vortex modes with azimuthal order $\ell = \pm 1$, described in Section III-B.

As can be seen, the target OAM state purity decreases relatively fast as the wavelength deviates from the target value of 1550 nm. Nevertheless, within the ± 5 nm wavelength region, the normalized power of OAM state ± 1 is still >0.9. However, with the further wavelength deviation, the OAM spectrum degrades dramatically, and at the wavelength deviation of ± 10 nm the normalized power of vortex modes with target OAM states drops down to about 0.5 with the prominent increase of conjugate vortex modes (i.e., with azimuthal order opposite to the target one).

IV. Discussion and Conclusions

As modeling results have shown, the proposed design of the integrated device can provide in-plane generation of the vortex mode with azimuthal order $\ell = \pm 1$ in rectangular dielectric waveguides compatible with the standard planar nanofabrication technology. Here we consider the symmetric silica-cladded silicon nitride waveguides with shallowly etched gratings; however, by correspondingly adjusting the GC parameters, the proposed design can be applied to various PIC technological platforms.

Compared to the other previously proposed schemes of integrated devices for vortex beam generation, the proposed design is characterized by the following: i) the output vortex mode is a pure phase vortex of quasi-TE polarization (not a vector vortex beam), where the helical phase front is carried by the dominant transverse electric field component; ii) excitation of the device is provided by a single standard SMF, which can be coupled in a technologically convenient in-line way using fiber array with angled facet; iii) no external electrical control or adjustment is needed for proper device operation, i.e., it can be implemented as a passive PIC.

Numerical modeling has shown that the generated vortex modes have normalized power coefficients of target OAM states ± 1 higher than 0.96, which is sufficient for most applications. At the same time, the calculated coupling efficiency of the proposed GC design (about 2%) is relatively low compared to the typical values of the conventional GCs for fundamental TE_{00} mode excitation. This is mainly a consequence of relatively low coupling efficiency to the TE_{10} eigenmode, especially if we target the possibly highest OAM state purity, and thus the parasitic excitation of other higher-order modes needs to be supressed (see Fig. 3 a,c).

However, here the GC parameters have been optimized approximately in a manual way, and probably the use of modern optimization algorithms can provide the precise global optimal values for the set of objective functions (4)–(7). Therefore, both OAM state purity and the coupling efficiency for the output waveguide mode could be further increased. Additionally, etching depth is a free GC parameter, which can also be varied to optimize the GC performance.

Moreover, the coupling efficiency can be further optimized using apodization for matching the GC scattering profile to the mode field distribution in SMF [26], [37], as well as by utilizing a bottom reflector based on a grating [38] or distributed Bragg reflector [39]. According to our theoretical predictions, proper 2-dimensional apodization for our GC design can provide

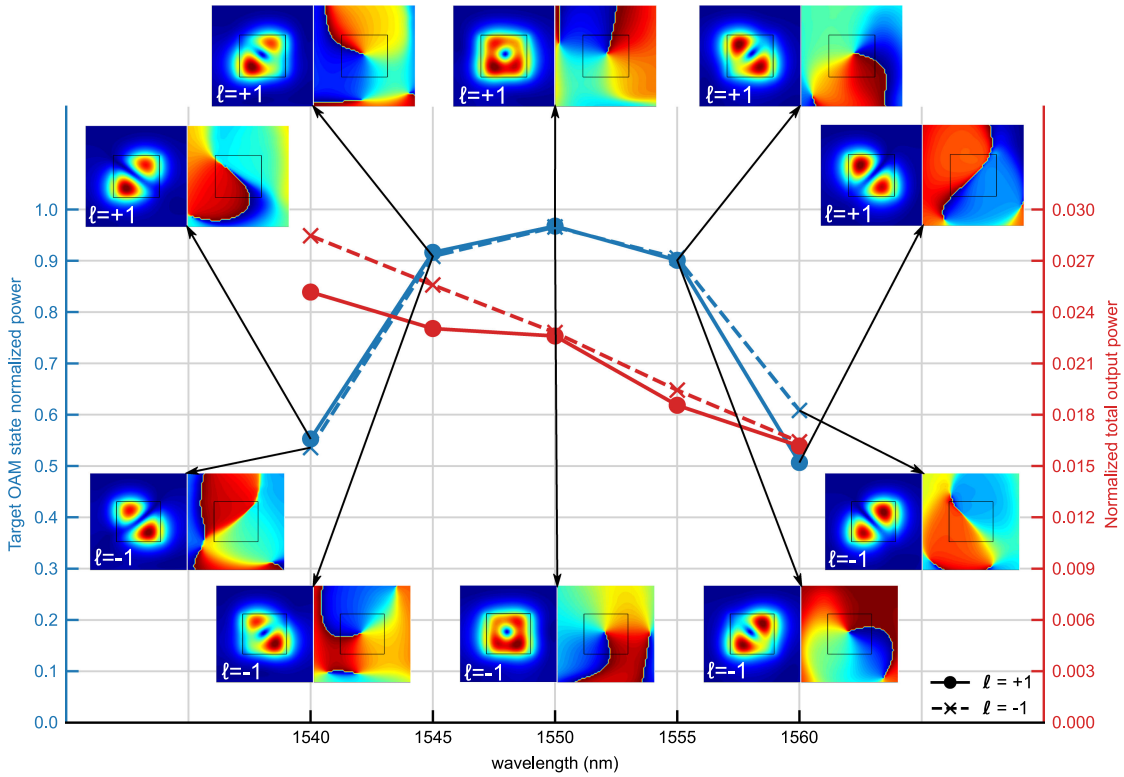

Fig. 9. Normalized power of the target OAM states ± 1 and the normalized total power at the device output depending on the wavelength. The insets show the corresponding amplitude and phase distributions of the E_x field component in the target waveguide.

about two times improvement in coupling efficiency. Using the bottom reflector, according to the results shown in [38], [39], can increase the coupling efficiency by up to 1.8 times. Therefore, applying these means to the proposed GC design is supposed to provide approximately 8% (i.e., about –11 dB) coupling efficiency without a reduction of the output OAM state purity.

From the fabrication point of view, the periods and relative shift of the sub-gratings in the GC can be set precisely, whereas the etching depth and filling factor of the fabricated devices may deviate from the designed values, depending on the conditions of a technological process. Therefore, the proper device design with the optimized set of GC parameters can be implemented via a two-run fabrication cycle: at the 1st run the test GCs with swept parameters would be fabricated to analyze the real geometry of the etched features, and at the 2nd run the GC parameters could be accordingly adjusted in order to get the fabricated devices with the designed geometry.

ACKNOWLEDGMENT

Authors thank Valeriy Kh. Bagmanov for fruitful discussions. Authors also thank the Institute of Computer Studies of the Ufa State Aviation Technical University for providing the supercomputer cluster for performing the numerical calculations.

REFERENCES

[1] L. Allen, M. W. Beijersbergen, R. Spreeuw, and J. Woerdman, "Orbital angular momentum of light and the transformation of Laguerre-Gaussian laser modes," *Phys. Rev. A*, vol. 45, no. 11, pp. 8185–8189, 1992.

[2] N. Bozinovic *et al.*, "Terabit-scale orbital angular momentum mode division multiplexing in fibers," *Science*, vol. 340, no. 6140, pp. 1545–1548, 2013.

[3] L. Gong *et al.*, "Optical orbital-angular-momentum-multiplexed data transmission under high scattering," *Light: Sci. Appl.*, vol. 8, no. 1, pp. 1–11, 2019.

[4] F. Zhu *et al.*, "Free-space optical communication link using perfect vortex beams carrying orbital angular momentum (OAM)," *Opt. Commun.*, vol. 396, pp. 50–57, 2017, https://doi.org/10.1016/j.optcom.2017.03.023.

[5] G. Xie *et al.*, "Experimental demonstration of a 200-gbit/s free-space optical link by multiplexing Laguerre-Gaussian beams with different radial indices," *Opt. Lett.*, vol. 41, no. 15, pp. 3447–3450, 2016.

[6] V. S. Vasilev, A. I. Kapustin, R. V. Skidanov, N. A. Ivliev, V. V. Podlipnov, and S. V. Ganchevskaya, "Experimental investigation of the stability of bessel beams in the atmosphere," *Comput. Opt.*, vol. 43, no. 3, pp. 376–384, 2019.

[7] M. Padgett and R. Bowman, "Tweezers with a twist," *Nature Photon.*, vol. 5, no. 6, pp. 343–348, 2011.

[8] Y. Zhang *et al.*, "Nonlinearity-induced multiplexed optical trapping and manipulation with femtosecond vector beams," *Nano Lett.*, vol. 18, no. 9, pp. 5538–5543, 2018.

[9] L. Gong, B. Gu, G. Rui, Y. Cui, Z. Zhu, and Q. Zhan, "Optical forces of focused femtosecond laser pulses on nonlinear optical Rayleigh particles," *Photon. Res.*, vol. 6, no. 2, pp. 138–143, 2018.

[10] S. Fürhapter, A. Jesacher, S. Bernet, and M. Ritsch-Marte, "Spiral phase contrast imaging in microscopy," *Opt. Exp.*, vol. 13, no. 3, pp. 689–694, 2005.

[11] K. I. Willig, S. O. Rizzoli, V. Westphal, R. Jahn, and S. W. Hell, "Sted microscopy reveals that synaptotagmin remains clustered after synaptic vesicle exocytosis," *Nature*, vol. 440, no. 7086, pp. 935–939, 2006.

[12] C. Zhang, C. Min, L. Du, and X.-C. Yuan, "Perfect optical vortex enhanced surface plasmon excitation for plasmonic structured illumination microscopy imaging," *Appl. Phys. Lett.*, vol. 108, no. 20, p. 201601, 2016, https://doi.org.proxylib.skoltech.ru:2050/10.1063/1.4948249.

[13] T. Stav *et al.*, "Quantum entanglement of the spin and orbital angular momentum of photons using metamaterials," *Science*, vol. 361, no. 6407, pp. 1101–1104, 2018.

[14] M. Malik, M. Erhard, M. Huber, M. Krenn, R. Fickler, and A. Zeilinger, "Multi-photon entanglement in high dimensions," *Nature Photon.*, vol. 10, no. 4, pp. 248–252, 2016.
[15] N. Cvijetic, G. Milione, E. Ip, and T. Wang, "Detecting lateral motion using light's orbital angular momentum," *Sci. Rep.*, vol. 5, 2015, Art. no. 15422.
[16] S. Khonina, N. Kazanskiy, and V. Soifer, "Optical vortices in a fiber: Mode division multiplexing and multimode self-imaging," *Recent Prog. Opt. Fiber Res.*, no. 65-P, pp. 327–352, 2012, pp. 1–7, https://doi.org/10.1038/srep15422.
[17] J. Courtial and M. Padgett, "Performance of a cylindrical lens mode converter for producing Laguerre-Gaussian laser modes," *Opt. Commun.*, vol. 159, no. 1-3, pp. 13–18, 1999, https://doi.org/10.5772/28067.
[18] M. Beijersbergen, R. Coerwinkel, M. Kristensen, and J. Woerdman, "Helical-wavefront laser beams produced with a spiral phaseplate," *Opt. Commun.*, vol. 112, no. 5-6, pp. 321–327, 1994.
[19] N. Heckenberg, R. McDuff, C. Smith, and A. White, "Generation of optical phase singularities by computer-generated holograms," *Opt. Lett.*, vol. 17, no. 3, pp. 221–223, 1992.
[20] R. Li, X. Feng, D. Zhang, K. Cui, F. Liu, and Y. Huang, "Radially polarized orbital angular momentum beam emitter based on shallow-ridge silicon microring cavity," *IEEE Photon. J.*, vol. 6, no. 3, Jun. 2014, Art. no. 2200710.
[21] X. Cai *et al.*, "Integrated compact optical vortex beam emitters," *Science*, vol. 338, no. 6105, pp. 363–366, 2012.
[22] Z. Xie *et al.*, "Ultra-broadband on-chip twisted light emitter for optical communications," *Light: Sci. Appl.*, vol. 7, no. 4, pp. 18001–18001, 2018.
[23] H. Li *et al.*, "Orbital angular momentum vertical-cavity surface-emitting lasers," *Optica*, vol. 2, no. 6, pp. 547–552, 2015.
[24] D. Zhang, X. Feng, and Y. Huang, "Encoding and decoding of orbital angular momentum for wireless optical interconnects on chip," *Opt. Exp.*, vol. 20, no. 24, pp. 26986–26995, 2012.
[25] Y. Wang *et al.*, "Integrated photonic emitter with a wide switching range of orbital angular momentum modes," *Sci. Rep.*, vol. 6, 2016, Art. no. 22512.
[26] Z. Zhao and S. Fan, "Design principles of apodized grating couplers," *J. Lightw. Technol.*, vol. 38, no. 16, pp. 4435–4446, Aug. 2020, https://doi.org/10.1038/srep22512.
[27] J. Liu *et al.*, "Orbital angular momentum modes emission from a silicon photonic integrated device for km-scale data-carrying fiber transmission," *Opt. Exp.*, vol. 26, no. 12, pp. 15471–15479, 2018.
[28] S. Li *et al.*, "Orbital angular momentum vector modes (de) multiplexer based on multimode micro-ring," *Opt. Exp.*, vol. 26, no. 23, pp. 29 895–29 905, 2018.
[29] S. Zheng and J. Wang, "On-chip orbital angular momentum modes generator and (de) multiplexer based on trench silicon waveguides," *Opt. Exp.*, vol. 25, no. 15, pp. 18492–18501, 2017.
[30] Y. Liang, H. W. Wu, B. J. Huang, and X. G. Huang, "Light beams with selective angular momentum generated by hybrid plasmonic waveguides," *Nanoscale*, vol. 6, no. 21, pp. 12360–12365, 2014.
[31] Y. Liang, F. Zhang, J. Gu, X. G. Huang, and S. Liu, "Integratable quarter-wave plates enable one-way angular momentum conversion," *Sci. Rep.*, vol. 6, 2016, Art. no. 24959.
[32] F. C. Ni, Z. T. Xie, X.-d. Hu, C.-y. Jia, and X. G. Huang, "Selective angular momentum generator based on a graphene hybrid plasmonic waveguide," *J. Lightw. Technol.*, vol. 37, no. 21, pp. 5486–5492, 2019, https://doi.org/10.1038/srep24959.
[33] Y. Meng *et al.*, "Versatile on-chip light coupling and (de) multiplexing from arbitrary polarizations to controlled waveguide modes using an integrated dielectric metasurface," *Photon. Res.*, vol. 8, no. 4, pp. 564–576, 2020.
[34] D. Zhang, X. Feng, K. Cui, F. Liu, and Y. Huang, "Generating in-plane optical orbital angular momentum beams with silicon waveguides," *IEEE Photon. J.*, vol. 5, no. 2, Apr. 2013, Art. no. 2201206.
[35] V. S. Lyubopytov, R. V. Kutluyarov, V. K. Bagmanov, N. Neumann, and A. K. Sultanov, "Modeling and optimization of vortex modes propagation in rectangular dielectric waveguides," *IEEE Photon. J.*, vol. 12, no. 1, Feb. 2020, Art. no. 6100117.
[36] E. Yao, S. Franke-Arnold, J. Courtial, S. Barnett, and M. Padgett, "Fourier relationship between angular position and optical orbital angular momentum," *Opt. Exp.*, vol. 14, no. 20, pp. 9071–9076, 2006.
[37] R. Marchetti *et al.*, "High-efficiency grating-couplers: Demonstration of a new design strategy," *Sci. Rep.*, vol. 7, no. 1, pp. 1–8, 2017.
[38] J. Zou, Y. Yu, M. Ye, L. Liu, S. Deng, and X. Zhang, "Ultra efficient silicon nitride grating coupler with bottom grating reflector," *Opt. Exp.*, vol. 23, no. 20, pp. 26305–26312, 2015.
[39] H. Zhang *et al.*, "Efficient silicon nitride grating coupler with distributed bragg reflectors," *Opt. Exp.*, vol. 22, no. 18, pp. 21800–21805, 2014.